

Supporting Information for “Strain partitioning and present-day fault kinematics in NW Tibet from Envisat SAR interferometry”

Simon Daout^{1,4}, Marie-Pierre Doin¹, Gilles Peltzer^{2,3}, Cécile Lasserre^{1,5}, Anne Socquet¹,
Matthieu Volat¹, Henriette Sudhaus⁴

¹Univ. Grenoble Alpes, Univ. Savoie Mont Blanc, CNRS, IRD, IFSTTAR, ISTerre, 38000 Grenoble, France

²Department of Earth Science, University of California, LA, USA

³Jet Propulsion Laboratory, California Institute of Technology, CA

⁴Christian-Albrecht-Universität zu Kiel, Department of Geosciences

⁵Univ Lyon, Université Lyon 1, ENS de Lyon, CNRS, UMR 5276 LGL-TPE, Villeurbanne, France

1 Introduction

We identified two main InSAR processing challenges in our area (Fig. S1). The first one concerns the effects of the seasonal deformation of the permafrost’s active layer in the Tibetan plateau (Fig. S1A), whilst the second one is linked to the trade-offs between quadratic residual orbital ramps, tropospheric delays and deformation across the topographic step (Fig. S1B). This supplementary material file provides more details explanations, illustrating our InSAR processing strategy, which is based on a series of corrections on the wrapped phase aimed at enhancing the tectonic deformation-to-noise ratio before the critical unwrapping phase. We also provide more details about the GPS data post-processing, as well as the model.

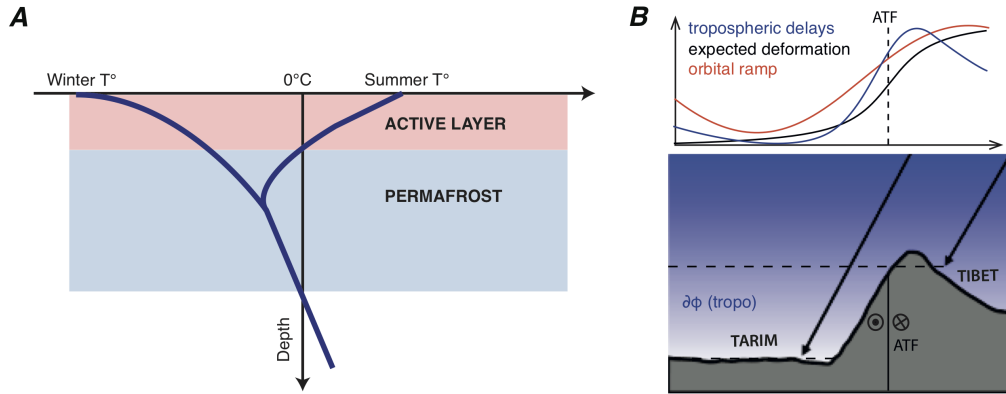


Figure S1. Schematic representation of the InSAR processing challenges in Tibet. A) Seasonal freeze and thaw cycles of the permafrost’s active layer. Typical depths of the active layers in Tibet range between 0.1 to 3 m. B) Trade-offs between tropospheric delays, orbital ramps and deformation across the Altyn Tagh Fault.

2 Choice of the interferometric network

For the four tracks we define an optimal small baseline interferometric network connecting with redundancy all acquisitions using perpendicular baseline constraint, B_{perp} , and temporal baseline constraint, B_t (Fig. S2). Note that, contrary to the traditional SBAS approach, some interferograms present either large B_{perp} and low B_t , to better estimate the DEM errors on the wrapped phase, as well as low B_{perp} and large B_t interferograms that connect full coverage acquisition together.

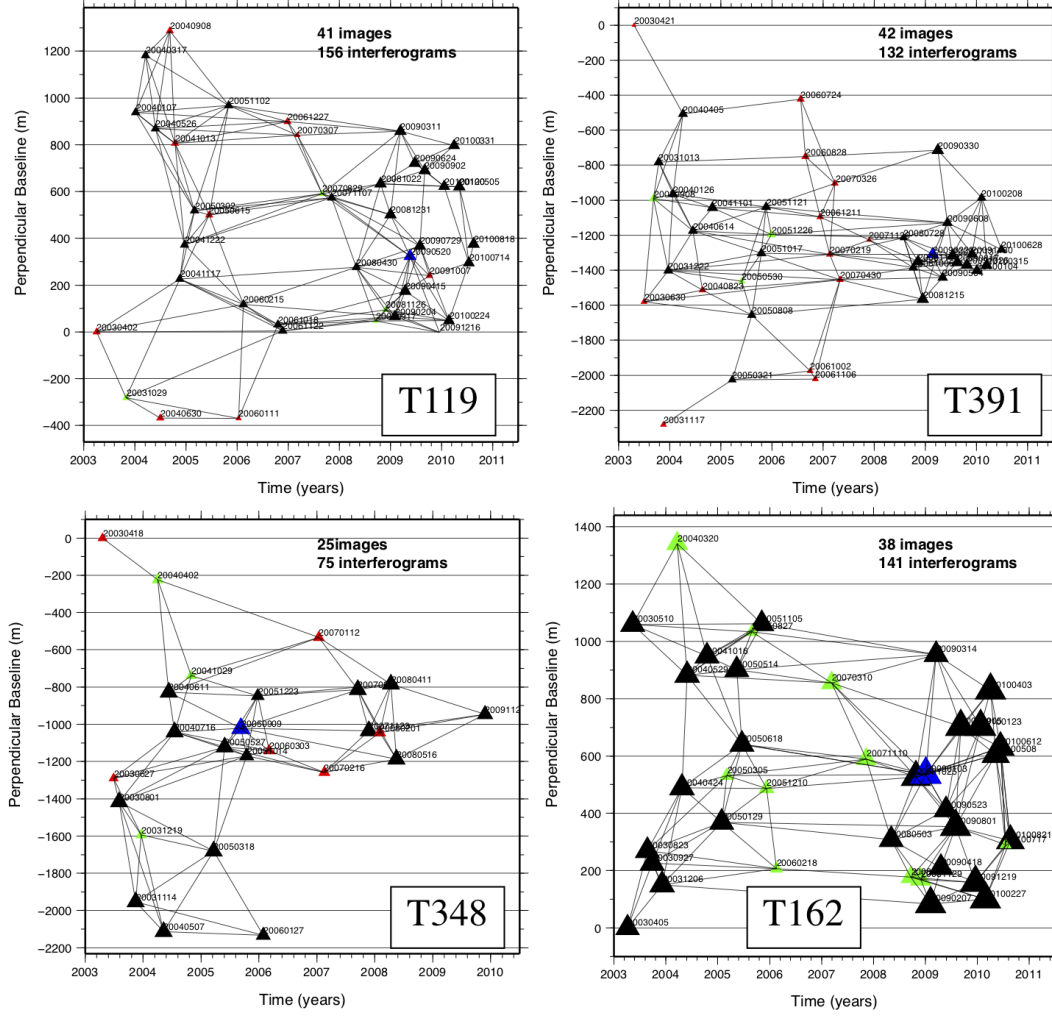


Figure S2. Computed interferograms for the four tracks. Triangles are SAR acquisitions with sizes and colors according to their spatial extent: black triangles for a full coverage, green triangles for images covering the northern part of the track only, and red colors for images covering the southern part only. The master image is shown with a blue triangle.

3 Local DEM error correction

Local Digital Elevation Model (DEM) errors are corrected before unwrapping using the method described in [Ducret *et al.*, 2014]. This correction is of particular importance in this area of high topography and because we perform interferograms with large B_{perp} . The impact of DEM error on phase can exceed π , thus appearing as decorrelation noise in the interferometric phase (Fig. S3).

Local DEM errors are estimated based on the relationship between interferometric phase and perpendicular baseline [Ducret *et al.*, 2014]. This correction step is applied on the wrapped interferograms after removal of predicted flat earth and topographic contributions. Note that for Envisat data the deformation does not trade-off with the DEM error correction as the perpendicular baseline does not drift with time.

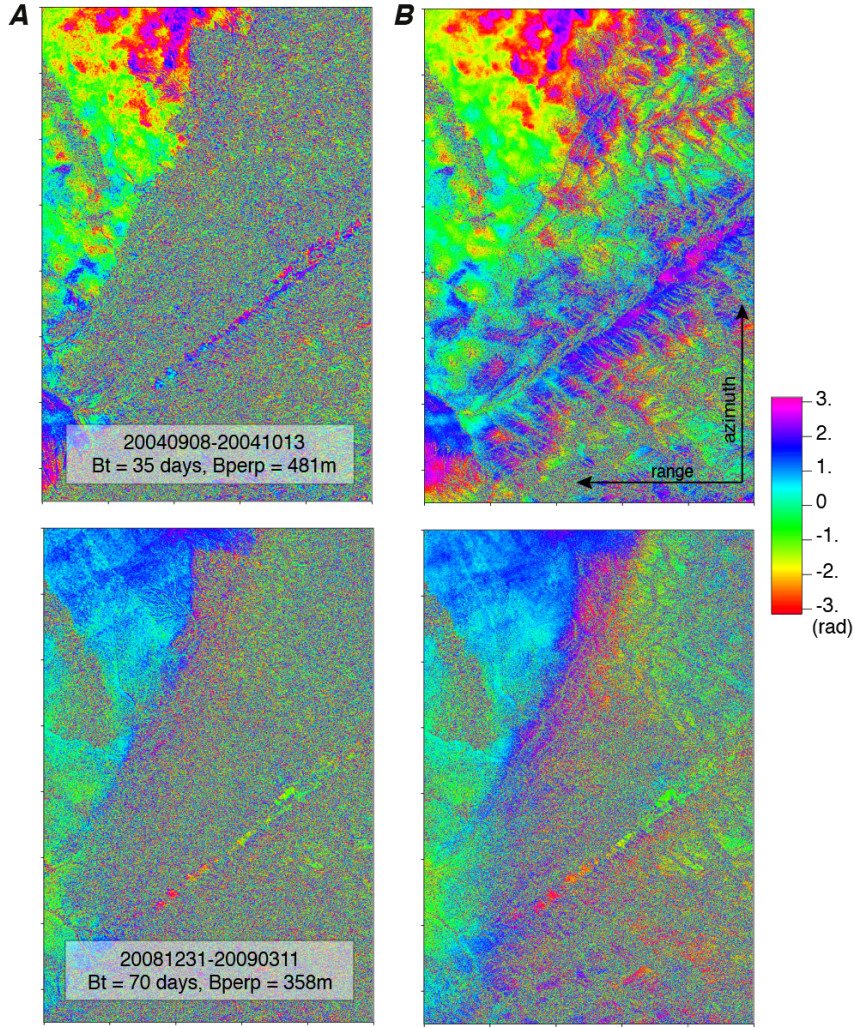


Figure S3. Two interferograms of track 119 with large perpendicular baseline across the Altyn Shans before (A) and after (B) local DEM errors correction.

To quantify the impact of the correction, we compute the local phase scatter before and after correction for all interferograms (Fig. S4). On average, the phase scatter of all interferograms decreases by 2.9% , but reaches up to 10-15% for large B_{perp} and low B_t interferograms. The average topographic error, $\delta h = \frac{\alpha \lambda \tan \theta}{4\pi}$, on the SRTM-derived DEM map in radar coordinate is of 1.9 m for the whole track.

4 Analysis of the atmospheric signal

We here focus more specifically on the analysis of the atmospheric signal in the radar phase correlated to elevation [Doin *et al.*, 2009; Jolivet *et al.*, 2011, 2014], which is the main source of errors for the extraction of small deformation signal in mountainous areas.

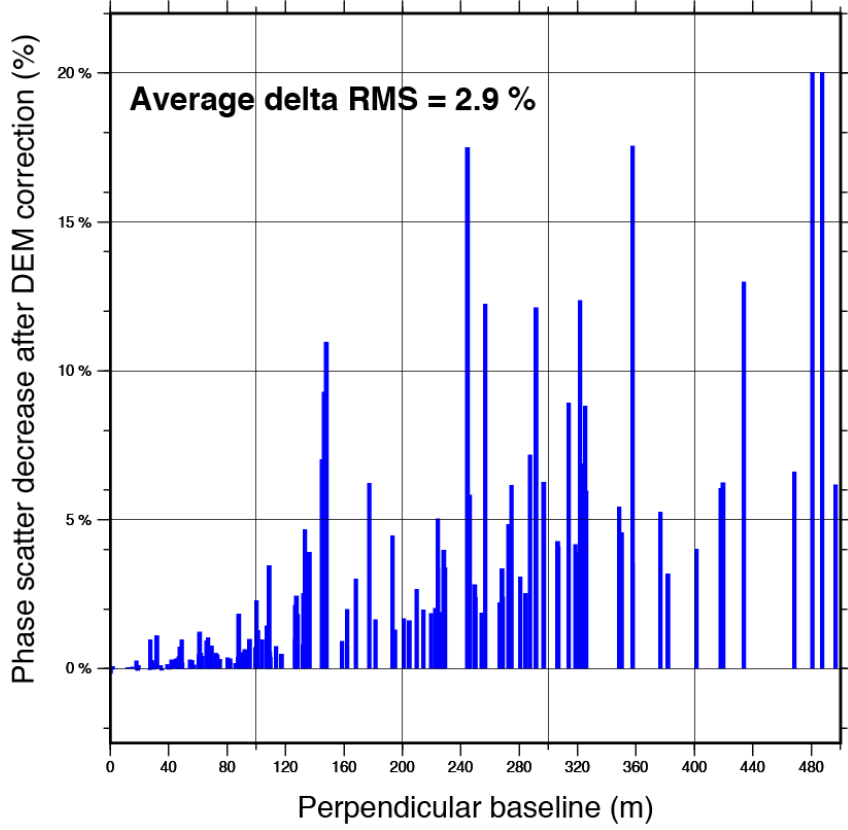


Figure S4. Phase scatter reduction, averaged in $\sim 50 \times 50$ pixel sub-windows, after DEM error correction for all 156 interferograms of track 119, as a function of perpendicular baseline.

4.1 Atmospheric corrections before unwrapping

The empirical estimation of the phase versus elevation relationship on the wrapped interferograms is done by searching the phase versus elevation ratio in small sub-windows, $\frac{\partial \phi}{\partial z}$, that maximises locally the coherence of the residual phase [Doin *et al.*, 2015]. The choice of local estimations on small sliding windows is motivated by the minimisation of possible trade-offs with the deformation, which is also correlated to the topography. By doing so, we emphasize local phase-elevation ratio due to valleys or gullies with respect to the long-wavelength phase-elevation ratio produced by the Altyn Tagh fault deformation. From all computed phase-elevation ratios, we select those obtained in sub-windows with good residual coherence and with a differential topography, Δz , larger than 150 m. We also decrease the weight of ratio values that are clear outliers and compute an average value, a , of all ratios. The empirical phase-elevation relationship is then:

$$\phi = az + b \quad (1)$$

In many interferograms, the delay-elevation ratios show a linear or quadratic correlation with elevation, as illustrated in Fig. S5. However, the choice of adjusting with only the average value is motivated by the minimisation of possible trade-off with the deformation.

Fig. S5 shows one example of a wrapped interferogram with a temporal baseline of 2.4 years and a perpendicular baseline of 72 m before and after empirical or predictive

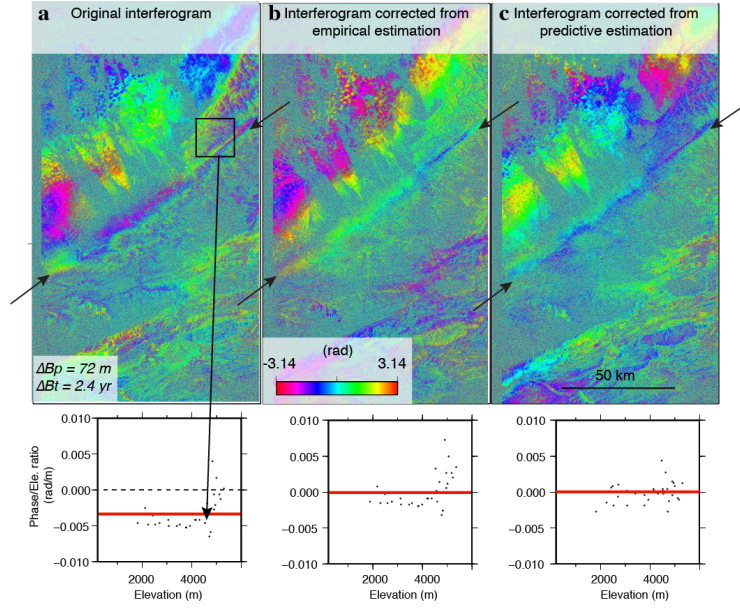


Figure S5. Comparison on an example of the empirical and the ERA-I corrections. Top: a: Wrapped interferogram with a temporal baseline of 2.4 years and a perpendicular baseline of 72 m. b: Same interferogram after empirical correction. c: Same interferogram after ERA-I correction. Bottom: Local phase-elevation ratios plotted as a function of elevation in original interferogram (a), after correction from empirical phase-elevation relationship (b) or after correction using ERA-I prediction (c). Each dot corresponds to a local estimate in a sub-window. The red line shows the average of all selected ratios.

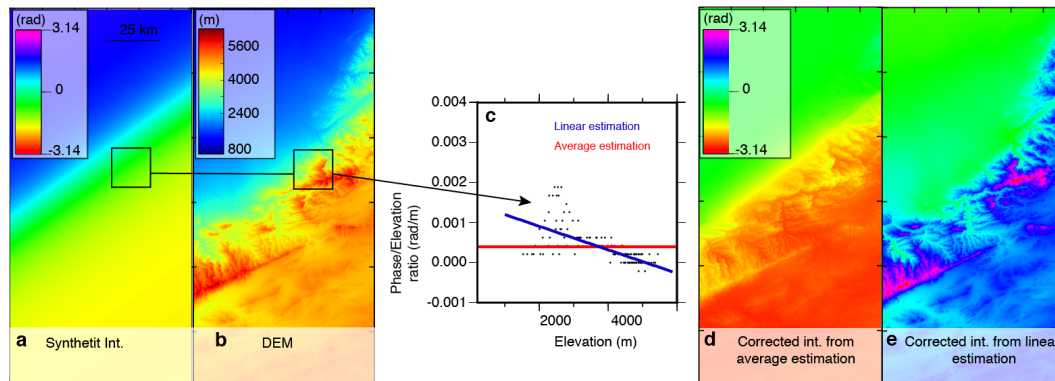


Figure S6. Empirical delay elevation relationship estimated on a synthetic interferogram with a temporal baseline of 5 years and simulated strike-slip motion of 15 mm/yr on the Altyn Tagh Fault locked until 15 km depth. (a) Synthetic interferogram. (b) Digital Elevation Model. (c) Delay-elevation ratios. The red and blue lines correspond to the average and linear estimations, respectively. Using a constant delay-elevation ratio removes part of the tectonic signal (d), while estimating a linear relationship removes all the tectonic signal on the synthetic interferogram (e).

atmospheric correction. Before the correction the short wavelength topographic structures are highlighted by phase changes, especially in the Altyn Shan, and the average delay-elevation ratio is -0.004 rad/m (i.e. ~ 5 cm for 3 km of topography). In this example, after both corrections, this stratified signal is in its majority removed and the delay-elevation

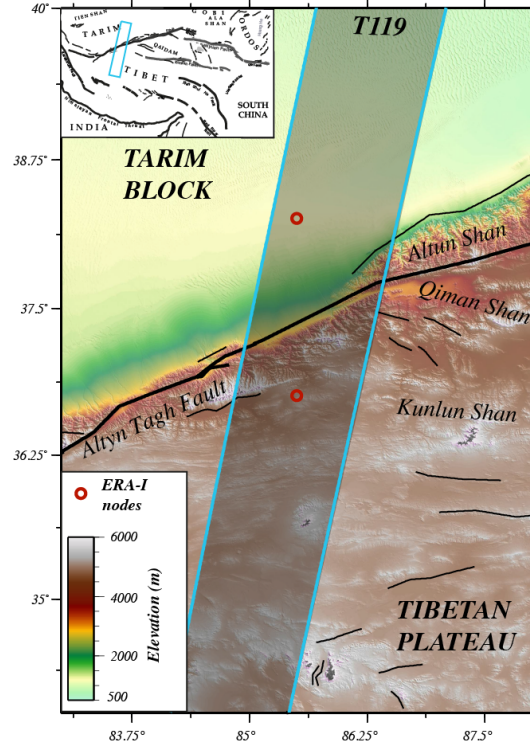


Figure S7. The two ERA-I nodes (red dots) used to estimate the atmospheric uncertainty in Fig. 2, superimposed on digital elevation model. The foot print of the track 119 and major fault traces are also drawn.

ratio is close to zero. However, some interferograms are not successfully corrected in one case or the other.

4.2 Trade-off between deformation and the tropospheric signal

To illustrate the possible trade-off of the empirical atmospheric correction with the tectonic signal, we simulate 5 years of strike-slip motion on a vertical half-infinite dislocation of 15 km depth aligned with the Altyn Tagh Fault surface trace (Fig. S6a) and estimate the delay elevation correlation on the synthetic interferogram (Fig. S6c-d). All phase-elevation ratios estimated within the Tibetan plateau with an altitude higher than 4 km are close to zero, while below this altitude, the ratios vary with elevation. The average of all delay-elevation ratios is close to zero (Fig. S6c), and the correction removes part of the tectonic signal (Fig. S6e). On the contrary, adjusting delay-elevation ratios with a linear or higher order relationship with elevation (Fig. S6d) gives weight to ratios at the foot of the ATF with delay/elevation ratios impacted by tectonic loading. We clearly see on Fig. S6f that this removes drastically the tectonic signal across the fault. Employing a power law relationship with elevation [Bekaert *et al.*, 2015] should lead to a similar trade-off. A wavelet transform analysis [Lin *et al.*, 2010; Shirzaei and Bürgmann, 2012] could

exploit the spatial heterogeneity of the phase-elevation relationship but depends on the completeness of the unwrapped signal in the area of interest. Here, empirical information on non tectonic phase-elevation relationship is basically missing due to the absence of small scale topographic features on the north side (low elevation part) of the fault. This synthetic example shows the ambiguity of empirical methods in a case where the deformation is strongly correlated to a large topographic feature. In comparison, predictive corrections do not have this disadvantage but suffer from the lack of accuracy in the daily delay estimation.

4.3 Validation of the ERA-I derived uncertainties using empirical estimates

In section 2.4 of the main text, we provide an error bound on ERA-I delay estimates based on its temporal variability. In the following, we discuss the reliability of this dispersion proxy, $\sigma_{p,i}^{ERA-I}$, showing that it corresponds well to a maximum error bound on ERA-I derived correction. This check is obtained by comparison with empirical phase-elevation ratios. The procedure is quite complex mainly because we do not have a direct access on the integrated empirical delay between Tarim and Tibet, which is the pertinent information provided by ERA-I.

Time series inversion of the delay-elevation ratios extracted from original interferogram yields the delay-elevation ratio at each acquisition date, $\left. \frac{\delta\phi}{\delta z} \right|_{EMP}$ [Doin *et al.*, 2009]. We first compare the empirical delay elevation from those computed on the ERA-I delay maps, $\left. \frac{\delta\phi}{\delta z} \right|_{ERA-I}$ (Fig. S8a). The dispersion of the empirical ratios obtained in various interferogram sub-windows is also inverted into time series assuming errors coming from both dates in the interferogram add up. It is displayed as error bars on the vertical axis on Fig. S8a. Note also that empirically derived $\left. \frac{\delta\phi}{\delta z} \right|_{EMP}$ may trade-off with orbital residual or deformation (section 3.2). Similarly, we compute error bars on $\left. \frac{\delta\phi}{\delta z} \right|_{ERA-I}$. We observe a very good agreement in between both estimations.

In order to infer a relationship between $\left. \frac{\delta\phi}{\delta z} \right|_{EMP}$ and $\Delta\phi_{Tibet-Tarim}^{EMP}$, we first examine the relationship between the phase difference between Tibet and Tarim, $\Delta\phi_{Tibet-Tarim}^{ERA-I}$ (in m), and the average delay-elevation ratios, $\left. \frac{\delta\phi}{\delta z} \right|_{ERA-I}$ (in rad/m), on ERA-I. (Fig. S8b). We observe a linear relation expressed by:

$$\Delta\phi_{Tibet-Tarim}^{ERA-I} = 2615 * \left. \frac{\delta\phi}{\delta z} \right|_{ERA-I} - 164, \quad (2)$$

Some acquisitions are clear outliers in Fig. S8b, indicating spatial variability of the atmospheric delays [Doin *et al.*, 2009; Bekaert *et al.*, 2015]. This relation is applied to compute an empirical estimate of $\Delta\phi_{Tibet-Tarim}^{EMP}$ from $\left. \frac{\delta\phi}{\delta z} \right|_{EMP}$ and of its standard deviation $\sigma_{\Delta\phi_{Tibet-Tarim}^{EMP}}$ from $\sigma_{\left. \frac{\delta\phi}{\delta z} \right|_{EMP}}$.

We then compare empirical delays between Tarim and Tibet, $\Delta\phi_{Tibet-Tarim}^{EMP}$, with the ERA-I predicted delay, $\Delta\phi_{Tibet-Tarim}^{ERA-I}$ (Fig. S8c). Fig. S8c presents more outliers than Fig. S8b. These outliers have a large $\sigma_{p,i}^{ERA-I}$ value, where $\sigma_{p,i}^{ERA-I}$ is the proxy discussed in the section 2.4 of the main text. These two observations suggest that ERA-I for these dates may not provide an accurate delay map estimate. Note that the 1σ error bar on $\Delta\phi_{Tibet-Tarim}^{ERA-I}$ in Fig. S8a-c encompass with few exceptions the defined regression line, suggesting that it represents a conservative estimate of errors. To further clarify this, we plot on Fig. S8d the time series of the empirical and ERA-I delays. The error bars on ERA-I delay estimates overlap the empirical delay estimates except for few dates. Four of these dates appear as anomalous values in the ERA-I time series, thus have large error bars, $\sigma_{p,i}^{ERA-I}$.

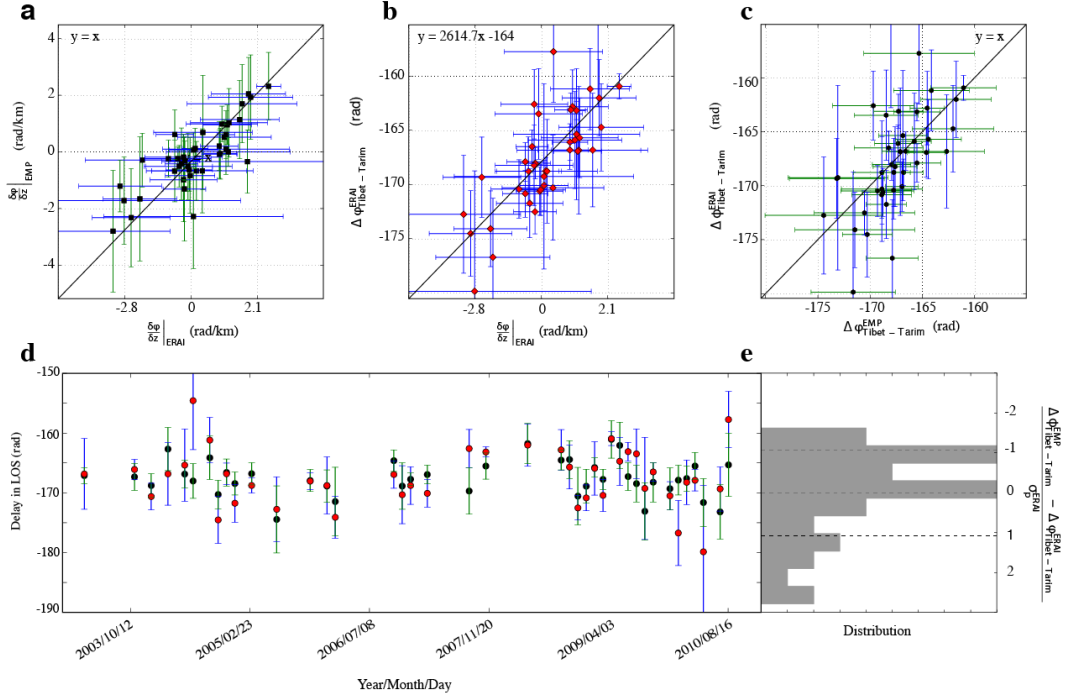


Figure S8. Comparison of the delay/elevation ratios estimated empirically on the InSAR data and those predicted by the ERA-I model, for each acquisition data. a) Comparison between the delay-elevation ratio estimated on the ERA-I maps and on the original interferograms. b) Comparison between predicted ERA-I phase delays between Tarim and Tibet, $\Delta\phi_{Tibet-Tarim}^{ERA-I}$, and estimated delay-elevation ratios on the computed ERA-I maps. c) Comparison between predicted ERA-I phase delay between Tarim and Tibet, $\Delta\phi_{Tibet-Tarim}^{ERA-I}$, and deduced phase delays from the empirical estimation, $\Delta\phi_{Tibet-Tarim}^{EMP}$. d) Relative delay-elevation ratios for the ERA-I model (red) and the data (black) plotted as a function of time. e) Distribution function for InSAR derived ratios minus the ERA-I predicted ratios, normalized by the dispersion proxy for ERA-I delay ratios.

We then display the histogram of InSAR derived delays, $\Delta\phi_{Tibet-Tarim}^{EMP}$, minus the delays predicted at acquisition dates, $\Delta\phi_{Tibet-Tarim}^{ERA-I}$, and normalised by their respective $\sigma_{p,i}^{ERA-I}$ uncertainties (Fig. S8e). Values remain concentrated within the $[-1.1, 1.1]$ interval, showing that the error proxy computed from 7-days variability of the ERA-I models is a conservative proxy for the uncertainties on the ERA-I predictions.

Finally, we provide the two stacks of empirical phase screen delay and ERA-I maps in Fig. S9b. We also quantify for the four tracks the velocity uncertainty across the ATF, $\sigma_{\Delta v}^{ERA-I}$, using the defined error proxy at each acquisition date to compute an error on the linear trend (Fig. S10). We quantify that ERA-I corrections add a velocity gradient of 0.55 rad/yr=2.45 mm/yr, -0.10 rad/yr=-0.46 mm/yr, 0.52 rad/yr=2.4 mm/yr, -0.45 rad/yr=-1.85 mm/yr across the ATF with an uncertainty of 0.19 rad/yr = 0.83 mm/yr, 0.21 rad/yr = 0.91 mm/yr, 0.18 rad/yr = 0.82 mm/yr and 0.29 rad/yr = 1.28 mm/yr, for the tracks 162, 391, 119 and 348, respectively.

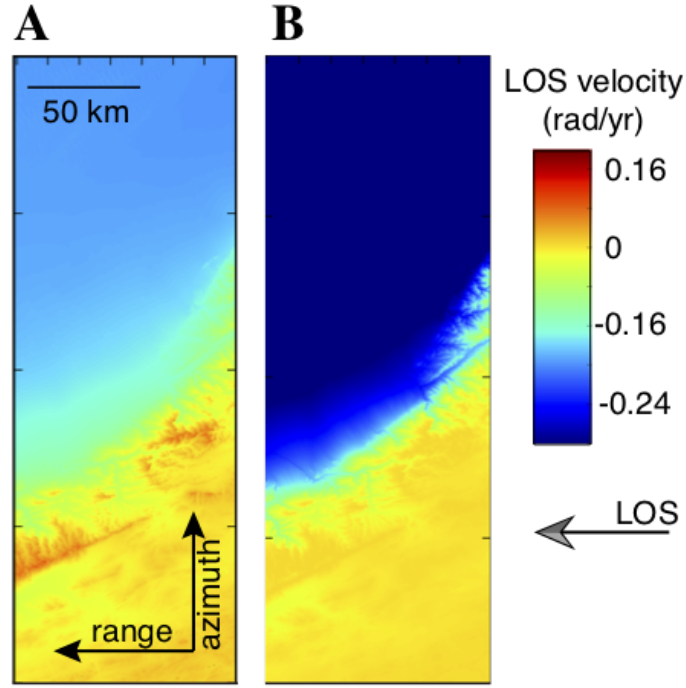


Figure S9. Comparison of the impact on the LOS velocity field of empirical correction [Doin *et al.*, 2015] (A) or of ERA-I correction based on one point located in the Tarim basin (B). The two velocity maps are obtained by weighting each image with their respective uncertainties derived from the empirical or ERA-I atmospheric analysis. A LOS velocity increase with elevation simulates a right-lateral movement.

5 Unwrapping and time series analysis

After performing the atmospheric and DEM corrections, the interferograms appear quite flat with some remaining smooth ramps and turbulent patterns albeit with abrupt phase patterns within the sedimentary basins due to permafrost freeze-thaw cycles [Daout *et al.*, 2017]. To unwrap the phase with confidence in all interferograms, we implement an iterative procedure by removing from the phase a template of deformation signal based on the Principal Component Analysis (PCA) of a first sub-series of correctly unwrapped interferograms (Fig. S11) [Daout *et al.*, 2017].

After this operation, the amplitude of the interferograms is replaced by the phase colinearity as defined by Pinel-Puysegur *et al.* [2012] and multi-looked by a factor of 8 and 40 in range and azimuth, respectively. A low-pass filter is then applied to the 8-looks interferograms, which is a weighted average of the complex phase in sliding windows. We observe an improvement of the unwrapping capability using two successive filters (Fig. S12) weighted by the average temporal coherence (Fig. S12a). Following López-Quiroz *et al.* [2009], we unwrap a smooth phase obtained with a strong low-pass filter (Fig. S12b) in order to help connecting areas separated by decorrelated zones. The unwrapping path goes from the high to the low coherence areas defined by the filter [Grandin *et al.*, 2012; Doin *et al.*, 2015]. We then compute the complex phase difference between the smoothed set of interferograms (Fig. S12b) and a second set of less-filtered interferograms (Fig. S12c). The residual high frequency signal is assumed to be between $-\pi$ and π and added to the previously unwrapped phase. We observe an improvement of the unwrapping capability across the alluvial fans and a reduction of unwrapping errors

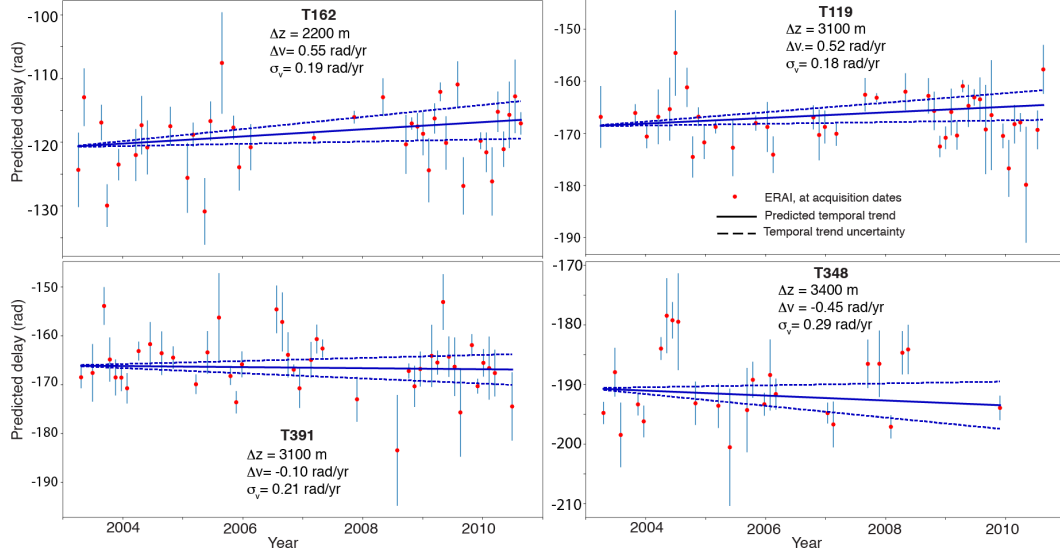


Figure S10. Relative delay in between the Tibetan plateau and the Tarim Basin (red circles) with associated error bar proxies (blue bars), $\sigma_{p,i}^{ERA-I}$, for the four tracks. Temporal trends (black lines), Δv^{ERA-I} , and uncertainties (black dashed-lines), $\sigma_{\Delta v}^{ERA-I}$, across the ATF due to the atmosphere from ERA-I models weighted by the defined proxy.

(Fig. S12e). At the end, the scaled template previously removed (based on the PCA) is added back to each interferogram to reconstruct the full unwrapped phase signal.

5.1 Residual orbital errors estimation

Before computing the time series analysis, it is necessary to remove an empirically determined long spatial wavelength to all interferograms in order to define a common reference for all interferograms (Fig. S13). However, some interferograms might present some residual atmospheric patterns or seasonal deformations in the referenced area that strongly affect the estimation of the long-wavelength spatial ramp. To overcome this difficulty, we mask the northern part of the Tarim Basin as well as permafrost areas with strong seasonal deformations, and determine the empirical azimuthal ramp in all interferograms. We also impose the closure of these long-wavelength azimuthal ramps within the interferometric network. Depending on the footprint length of both acquisitions used to compute interferogram (footprint restricted in the North or in the South of the track (Fig. S2)), the ramp is estimated with a linear or a quadratic term and is valid within the footprint extension. The inversion into time series of these ramps to obtain a ramp per acquisition is thus slightly unusual and implies extrapolation outside the valid interval for shorter images with a decreasing weight [Doin *et al.*, 2015]. At the end, all the ramps present a small quadratic coefficient.

5.2 Time series analysis and referencing of the four tracks

After the steps previously described, we analyse in time series the set of deramped unwrapped interferograms [López-Quiroz *et al.*, 2009; Doin *et al.*, 2011, 2015]. In the first run, the misclosure of the interferometric network is computed for each interferogram. If large, we visually check the corresponding interferogram and correct manually its unwrapping errors by imposing a new unwrapping path. In the final run, the unwrapping errors are automatically corrected using the network redundancy [López-Quiroz *et al.*, 2009; Doin

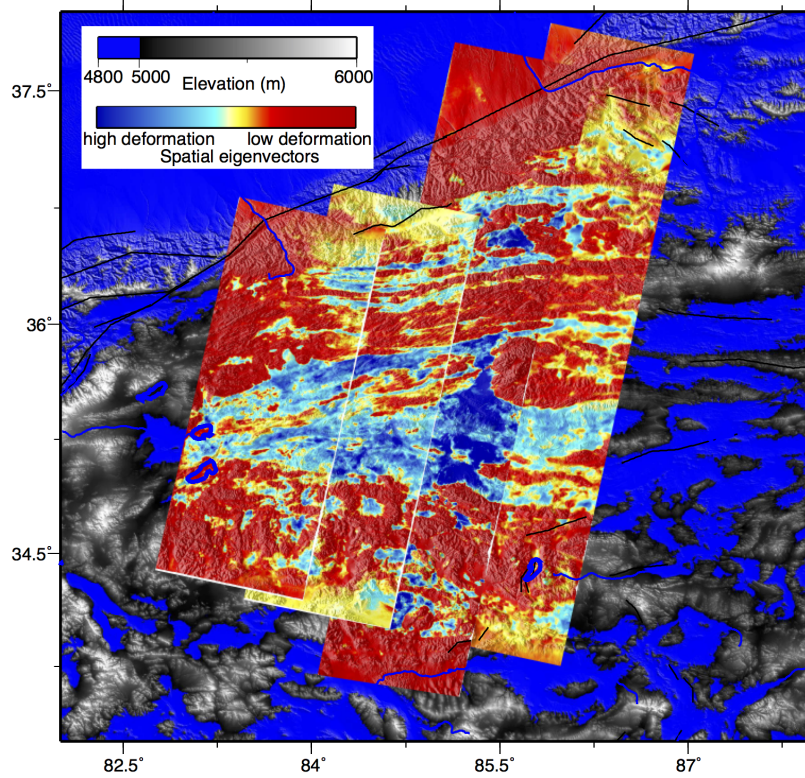


Figure S11. Spatial eigenvectors associated to the PCA component that present a strong seasonality [Daout *et al.*, 2017]. Blue patterns are deforming basins while red colors highlight stable bedrock. These maps are used as templates to unwrap interferograms.

et al., 2011]. The maximal RMS of final network inconsistencies at the end of this procedure is lower than ~ 0.7 rad for all interferograms. Incremental phase delay of each date relative to the preceding date is solved by a least square method. We observe on some tracks (mostly tracks 119 and 348), residual ramps in range that follow quadratic polynomial shape homogeneous from north to south. Before we extract the ground velocity displacement and the residual DEM error contribution (Figs. S15, S14), we refer each map, i , to the stable bedrock (defined by the permafrost map) and remove a quadratic ramp in range per acquisition. Note that this ramp correction does not trade-off with deformation as it is uniform along azimuth on tracks.

As a final referencing step, map are referred to each other with a quadratic adjustment in azimuth computed in the overlapping parts of the four velocity maps, all projected along a single incidence angle of 23.5° (Fig. S15). Following [Wen *et al.*, 2012], we also compute the histograms of the spread of difference between overlapping areas (Fig. S15A) and use it to estimate velocity errors, σ , of 0.4, 0.6, and 0.8 mm/yr between tracks 162 and 391, tracks 391 and 119 and tracks 119 and 348, respectively.

5.3 Covariance calculation

To quantify the noise, we compute the variances and empirical covariances (Fig. S16) of the four tracks with the Kite software [Isken *et al.*, 2017], part of the Pyrocko project [Heimann *et al.*, 2017]. We select for the four tracks a rectangular patch in an area without

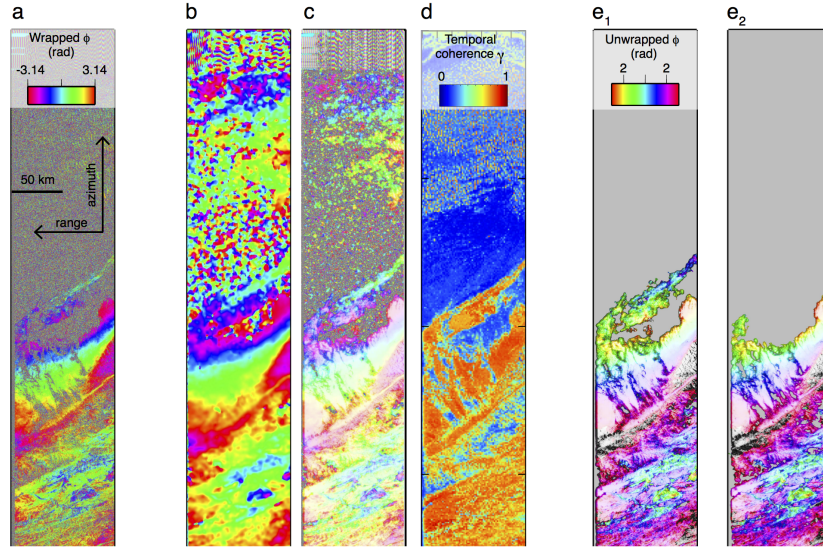


Figure S12. Example of an unwrapping procedure across the Tibet foreland. a: Multi-looked interferogram formed with the two images taken on Nov. 17, 2004 and on April 30, 2008. b, c: Interferograms after applying a low pass filter weighted by the average temporal coherence, γ , displayed in (d). The filter is stronger in (b) than in (c). Amplitude of (b) is used to define the unwrapping path of the interferograms shown in (c), resulting in a larger extent of the unwrapped surface. e: Two unwrapped interferograms obtained with a multi-looking weighted by (e_1) phase colinearity as defined by *Pinel-Puysegur et al.* [2012] or (e_2) by interferogram coherence.

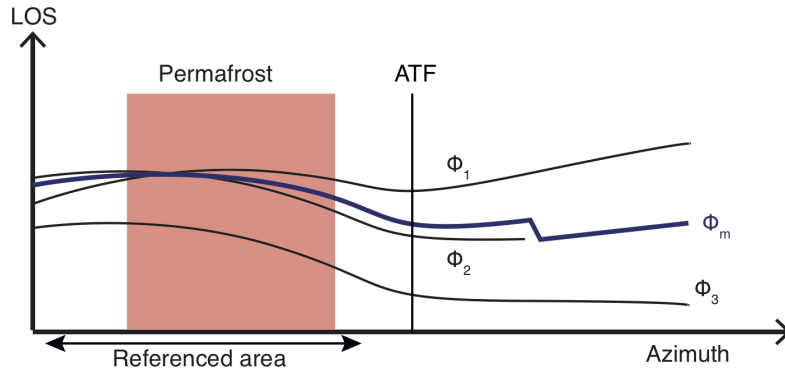


Figure S13. Schematic representation of the importance of referencing all interferograms to a common area before time series analysis. $\phi_{1,2,3}$ represent 3 interferograms with residual long spatial wavelengths and phase shift due to atmospheric patterns or seasonal deformations in the reference area. ϕ_m represents the stack of the 3 interferograms. Due to various lengths of the Envisat images and referencing errors, the stack might present artificial phase jumps in local zones.

deformation, between the ATF and the termination of the Manyi Fault. Variances (green dashed lines of Fig. S16) and empirical covariance (black lines of Fig. S16) are estimated directly from the power spectrum of displacement noise patch using the cosine transform [*Hanssen, 2001*].

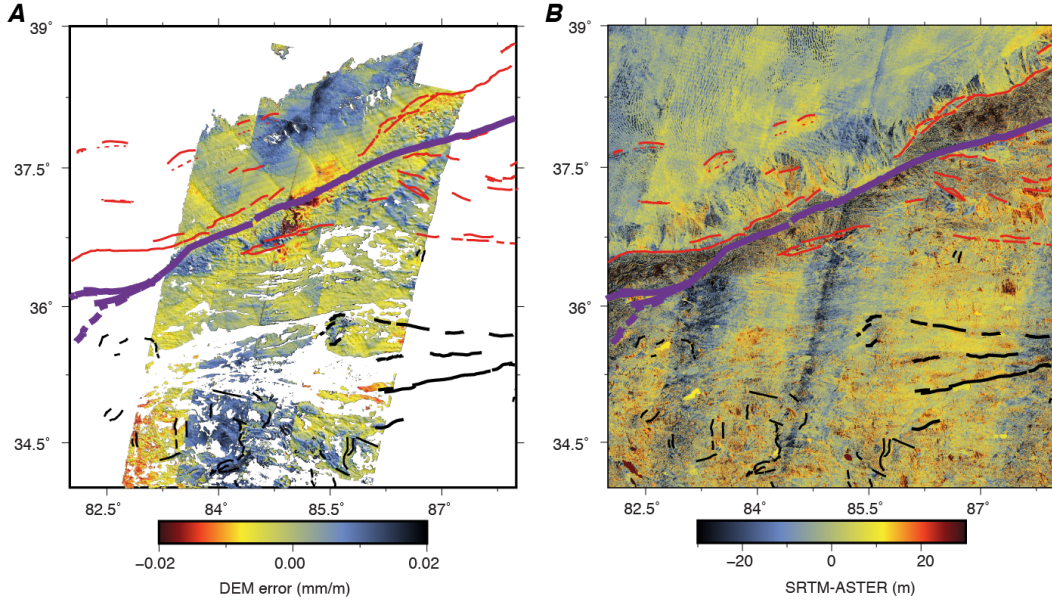


Figure S14. A: DEM error coefficients obtained from time series analysis in mm per meter of perpendicular baseline. Faults traces as Fig.1. B: Comparison with the difference between the DEM SRTM and DEM ASTER.

The velocity maps, which are extracted from time series analysis after multiple corrections that include multi-looking, phase averaging and filtering, show a low white noise and a covariance length about 2-3.5 km. Including the covariance between points in the inversion is computationally intensive and far from being the main source of errors here. Therefore, for the modelling part, we choose a data sub-sampling of ~ 3 km, higher than the noise characteristic correlation distance, in order to avoid taking into account the covariance between InSAR values.

6 GPS data

In order to compare the GPS field of Wang *et al.* [2017] with the GPS solution of He *et al.* [2013], we rotate the ITRF solution of Wang *et al.* [2017] with respect to the Tarim block, north of the ATF. To do so, we select 5 stations located in the Tarim Basin and far from the Altyn Tagh fault system (I033, I063, I064, XJTZ, and I065). Following the method described in Daout *et al.* [2016], we invert for an Euler pole by minimising the L1 norm of this subset of stations and apply the rotation to all GPS stations. He *et al.* [2013] referred their GPS velocities with respect to the stable Tarim block by minimising only three velocities of the sites AT12, AT13 and AT16. Note that the station AT13 is very close to the ATF while stations AT12 and AT16 are located on each side of the observed gradient of deformation of our InSAR velocity field in the Tarim Basin. This implies that the velocity field of He *et al.* [2013] is probably not exactly referenced with respect to the stable Tarim block, but with respect to a zone that undergoes some active deformation. As a consequence, despite our effort to rotate these velocity field in the same reference frame, a residual rotation may still remain between Wang *et al.* [2017]’s velocities (referred with respect to the stable Tarim), and He *et al.* [2013]’s velocities (referred with respect to sites located in an area shown to NE actively deforming). It is also worth noting that stations AT08, AT10, AT09 and AT11 are located at the termination of the

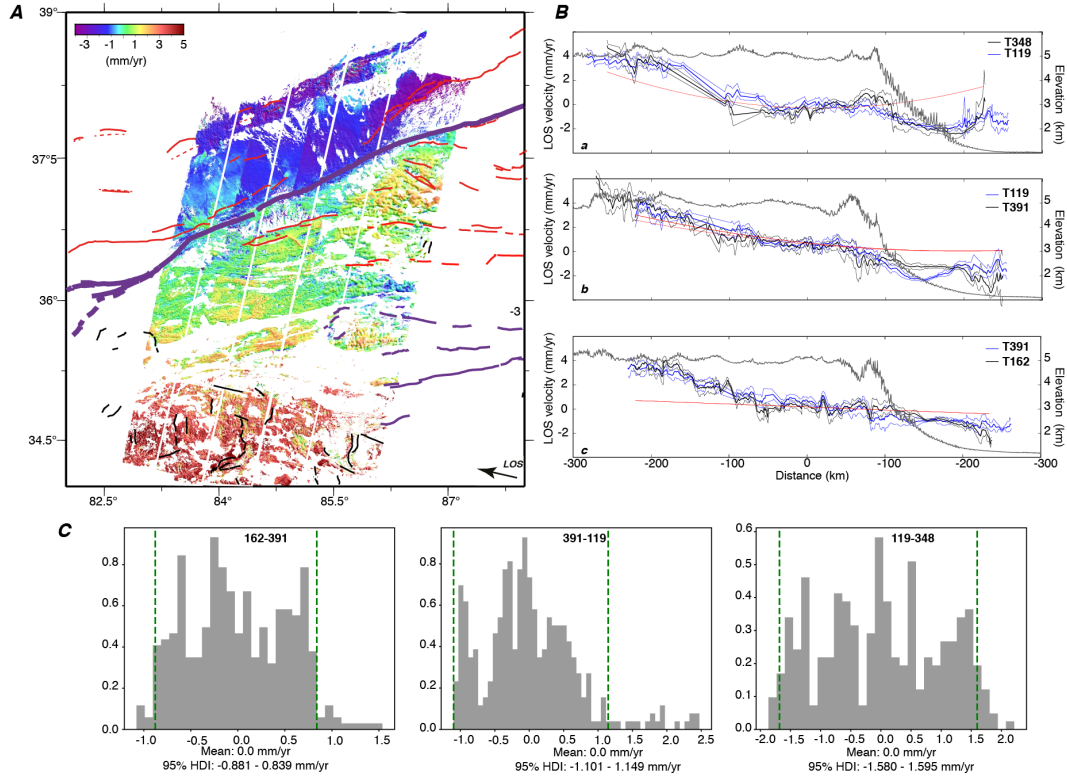


Figure S15. A: Line Of Sight velocity maps for the four tracks 162, 391, 119 and 348 displayed for an average incidence angle of 23.5° before the quadratic adjustment in azimuth minimising the differences between the tracks. B: Three profiles in the overlapping areas of the four tracks after the quadratic adjustment in azimuth. Red continuous lines correspond to estimated quadratic ramps minimising the differences between the tracks. Positive motion is toward the satellite. Faults traces as Fig.1. C: Histogram of differences between overlapping areas of the four tracks after quadratic adjustment and with associated 95% intervals.

Kunlun-Manyi fault, while stations AT01, AT02, AT03 and AT03A are within the Qiman Shan thrust system.

7 2D model across the ATF

We provide in Table S3 a summary of the prior and posterior probabilities for the three models discussed in section 4.2 of the main text constrained by various combinations of data sets. We also present the posterior correlation coefficient matrix in Fig. S18A and some selected joint-PDFs in Fig. S18B, illustrating the trade-offs between the model parameters. We also compare data and model in map-view in Fig. S17.

In order to support and explain the choice of the final model, we also provide preliminary models in Fig. S19, with smaller number of fault parameters than for the final model shown in Fig. 7. We also show in Fig. S20 another preliminary model that allows for both strike-slip and dip-slip motion on the ramp-décollement system and allows for a dip angle of the décollement.

Fig. S21 finally shows fault-parallel GPS velocities compared to models made of one single strike-slip semi-infinite dislocation with locking depths of 10, 20 and 30 km. The

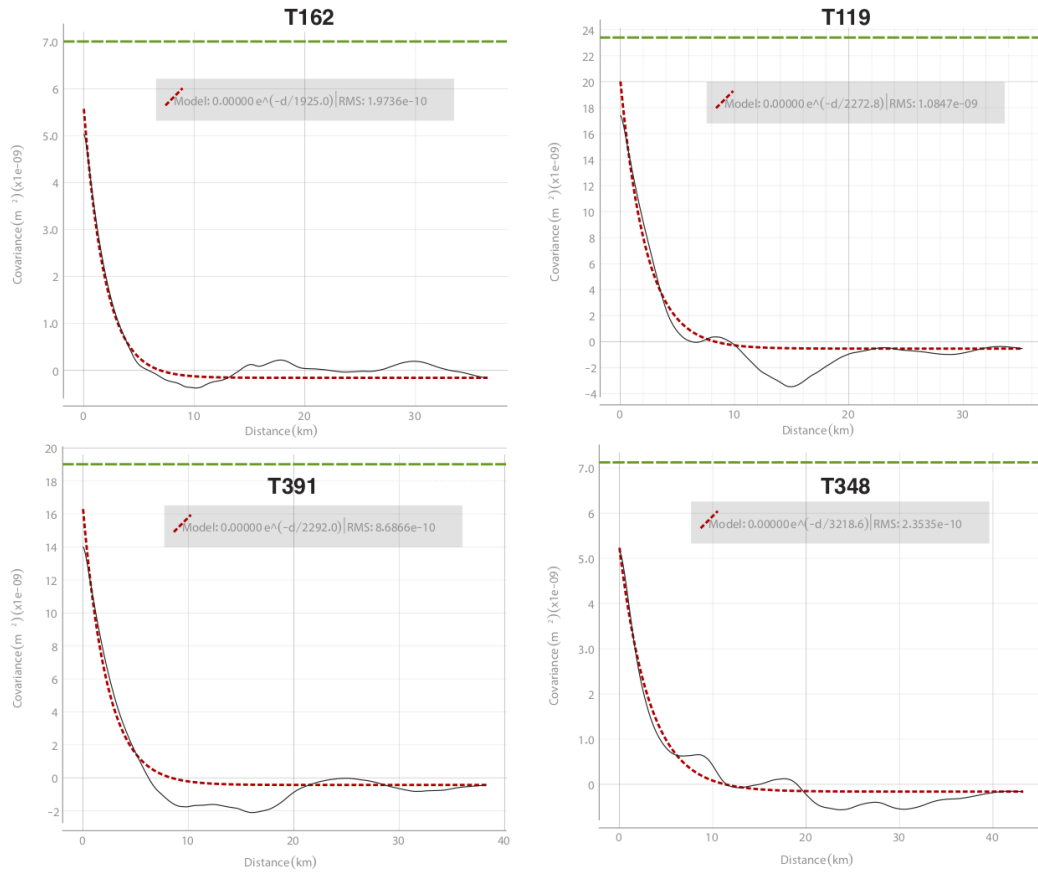


Figure S16. Variances (green dashed lines), empirical covariance (black lines) and associated best-fit exponential functions (red dashed lines) for the four tracks, computed on a selected area between the ATF and the western termination of the KF on the full resolution data set (180 m sampling).

range of modelled velocities values using these 3 locking depths are within the spread of GPS data.

Table S1. GPS velocity field from *He et al.* [2013] of Fig. 6 after referencing to the Tarim block and sorting by their fault-perpendicular distances to the ATF. Horizontal vectors are projected into the N66°E ATF-parallel (U_{par}) and ATF-perpendicular (U_{perp}) components to better visualize relative far-field shearing and shortening across the profile.

Station name	Lat.	Lon.	dist. (km)	U_{perp} (mm/yr)	U_{par} (mm/yr)
AT11	86.292	35.376	-226.8	3.298	-5.967
AT09	86.283	35.657	-197.3	2.265	-11.287
AT10	86.056	35.853	-169.6	1.990	-11.340
AT08	86.119	36.026	-153.7	-1.431	-9.434
AT07	86.056	36.253	-128.0	2.575	-7.714
AT06	86.250	36.428	-116.1	1.609	-8.926
AT05	86.317	36.575	-103.0	-0.248	-3.951
AT04	86.264	36.994	-57.8	-0.926	-8.104
AT03A	86.333	37.213	-37.2	-1.053	-8.365
AT03	86.309	37.232	-34.4	-2.695	-10.699
AT02	86.327	37.336	-24.2	-1.582	-7.659
AT01	86.380	37.413	-17.8	-0.946	-5.862
AT15	86.176	37.581	6.0	-1.002	-2.914
AT14	86.167	37.620	10.4	-0.989	-2.614
AT13	86.011	37.681	21.6	0.079	0.326
AT12	85.646	37.871	52.9	-0.128	-1.246
AT16	85.677	38.466	113.6	0.000	0.000

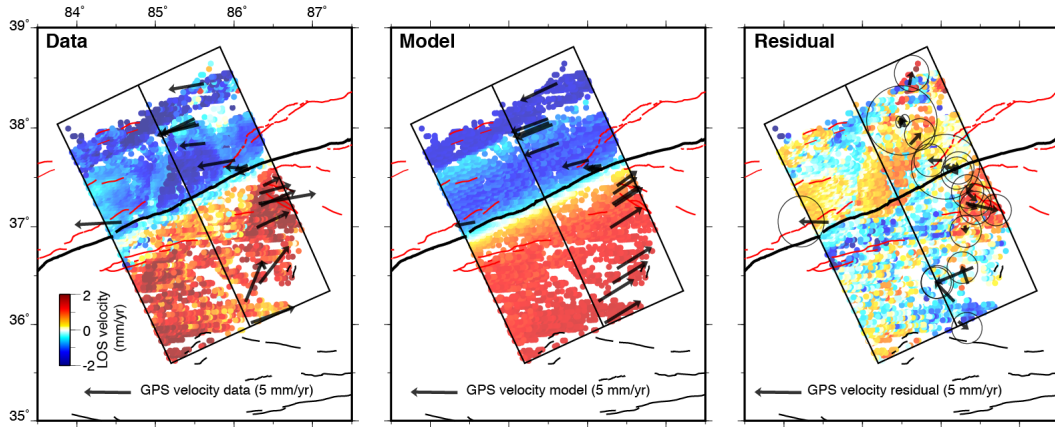


Figure S17. Comparison between data and model from the Bayesian inversion. Left: GPS and down-sampled InSAR data used for the inversion. InSAR data are down-sampled with Generic Mapping Tools (GMT) with a latitudinal and longitudinal increment of 0.0267°, respectively [Wessel and Smith, 1991], and then collapsed in the fault-perpendicular direction. Middle: Modelled displacements associated to the maximum likelihood of the posterior probability distribution. Right: Residuals between the forward model and the observations.

Table S2. As Table S2 for *Wang et al.* [2017]'s network.

Station name	Lat.	Lon.	dist. (km)	U_{perp} (mm/yr)	U_{par} (mm/yr)
J344	85.710	35.470	-197.9	4.460	-6.793
J343	84.830	35.470	-168.6	0.805	-6.182
J333	83.780	35.350	-145.1	2.498	-6.487
J325	82.800	35.020	-144.5	1.262	-6.287
I415	83.600	36.720	1.6	2.264	0.831
J408	86.170	37.590	7.2	-0.161	-0.312
I412	84.520	37.130	12.9	0.616	2.637
I069	82.990	36.740	24.7	2.427	1.886
XJYT	81.970	36.430	12.9	2.603	3.044
I067	82.700	37.050	66.4	2.000	1.813
I405	85.580	38.060	74.6	-0.513	2.068
I036	85.540	38.080	77.9	-0.927	2.197
I035	86.980	38.510	78.0	-2.224	1.986
XJQM	85.530	38.120	82.4	-1.464	1.604
I066	83.810	37.590	83.9	1.029	1.819
I034	88.180	39.020	95.9	-2.447	0.553
XJRQ	88.170	39.020	96.2	-3.599	1.701
I398	88.210	39.280	122.3	-2.890	1.648
I065	83.160	38.260	174.5	0.580	0.541
XJTZ	83.660	38.970	230.6	-0.212	0.138
I064	83.610	39.020	237.4	-0.981	-0.680
I033	88.250	40.270	315.4	-2.590	0.354
I063	84.340	40.220	337.3	0.000	0.000

Table S3. Summary of the prior and posterior probabilities for the three models (GPS data alone, InSAR data alone, joint inversion). \mathcal{U} defines uniform distribution. Posterior distributions are given by their 95% confidence intervals. V_{short} : shortening rate across the fault system; LD_{Shear} : depth of the tip of the deep-seated semi-infinite dislocation located at the triple junction between the ATF and the décollement; SS_{ATF} : strike-slip rate along the ATF; H_{ATF} : vertical distance between the tip of the shear zone and the tip of the ATF creeping segment; D_{Decol} , H_{Decol} : horizontal and vertical distances between the tip of the shear zone and the tip of décollement; D_{Ramp} , H_{Ramp} : horizontal and vertical distances between the tip of the décollement and the ramp tip. InSAR ramp corresponds to the linear coefficient.

variables	prior	posterior GPS	posterior InSAR	posterior GPS + InSAR
LD_{Shear} (km)	$\mathcal{U}(0, 80)$	39 [21, 53]	35 [29, 40]	35 [28, 41]
V_{short} (mm/yr)	$\mathcal{U}(0, 5)$	1.4 [0.0, 3.8]	0.9 [0.6, 1.2]	0.7 [0.5, 1.0]
SS_{ATF} (mm/yr)	$\mathcal{U}(0, 30)$	8.1 [6.6, 9.7]	13.3 [11.4, 15.1]	10.5 [9.4, 11.5]
H_{ATF} (km)	$\mathcal{U}(0, 40)$	31 [16, 40]	12 [4, 20]	17.6 [11.5, 24.5]
D_{Decol} (km)	$\mathcal{U}(0, 100)$	41 [10, 85]	62 [51, 72]	68 [60, 78]
D_{Ramp} (km)	$\mathcal{U}(0, 40)$	15 [0, 37]	29 [21, 38]	17 [6, 23]
H_{Ramp} (km)	$\mathcal{U}(0, 40)$	14 [0, 31]	31 [24, 37]	31 [23, 38]
T162 ramp (mm/yr/km)	$\mathcal{U}(-0.03, 0.03)$		-0.010 [-0.0122, 0.009]	-0.012 [-0.013, -0.011]
T391 ramp (mm/yr/km)	$\mathcal{U}(-0.03, 0.03)$		0.002 [0.0008, 0.0035]	0.0 [-0.001, 0.001]
T119 ramp (mm/yr/km)	$\mathcal{U}(-0.03, 0.03)$		0.006 [0.0047, 0.008]	0.003 [0.002, 0.004]
T348 ramp (mm/yr/km)	$\mathcal{U}(-0.03, 0.03)$		0.011 [0.010, 0.0126]	0.008 [0.001, 0.002]

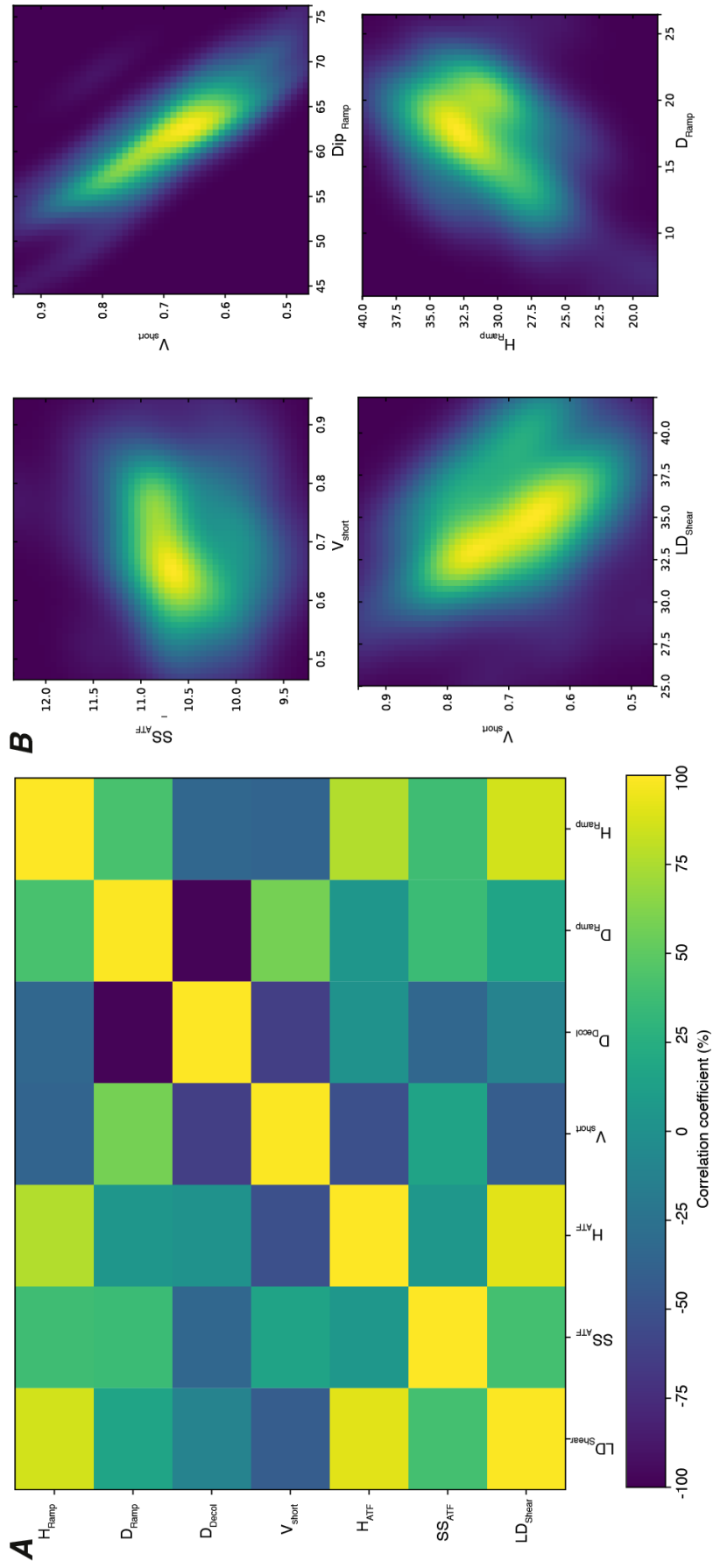


Figure S18. A: Posterior covariance matrix: correlation coefficient for all parameters. B: Joint PDFs between some correlated parameters. Interpretation in the main text.

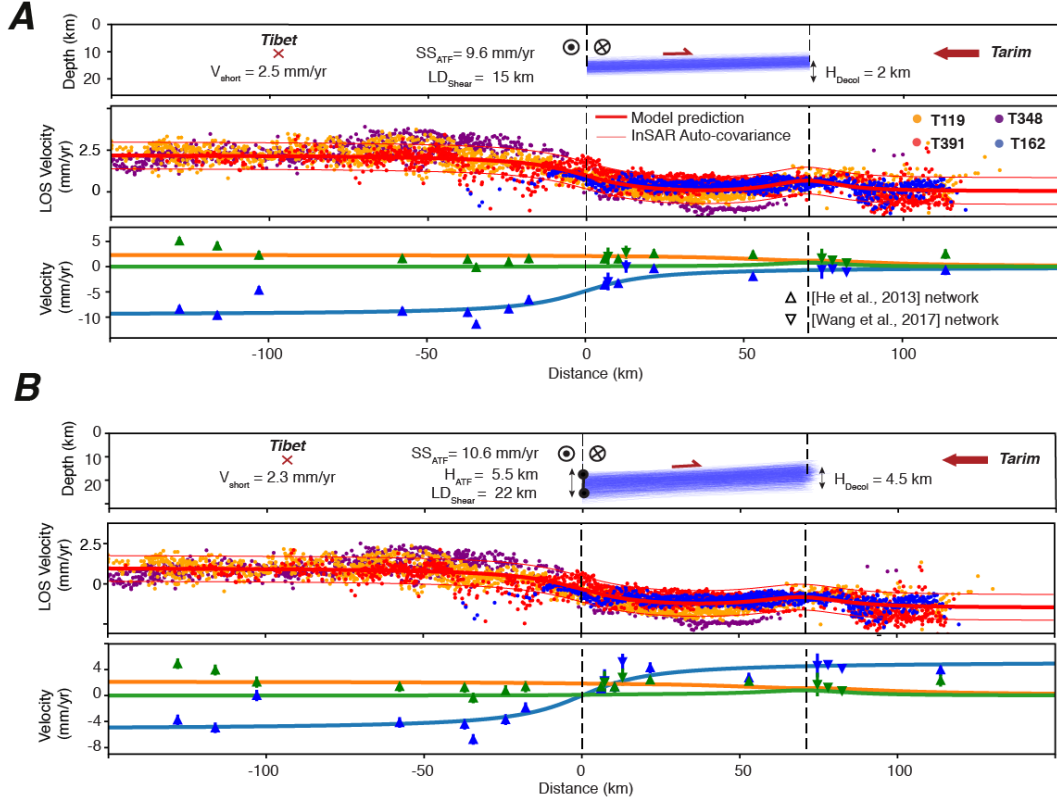


Figure S19. As Fig.7A but for models with less fault parameters. A: Model without a shallow creeping segment on the ATF above the décollement junction, with one décollement and without a frontal ramp. The model requires a shallow and low angle décollement and a high shortening rate. B: Model with a shallow creeping segment on the ATF above the décollement junction but without the frontal ramp. The model still requires a low-angle décollement and a high shortening rate, as a high décollement dip would create a strong vertical motion within the whole Tarim piedmont. Such models fail to explain the localised LOS velocity gradient observed at the base of the foreland fans in the Tarim Basin. The high shortening rate also seems too large in comparison to the limited amount geomorphological observations of convergence in this region.

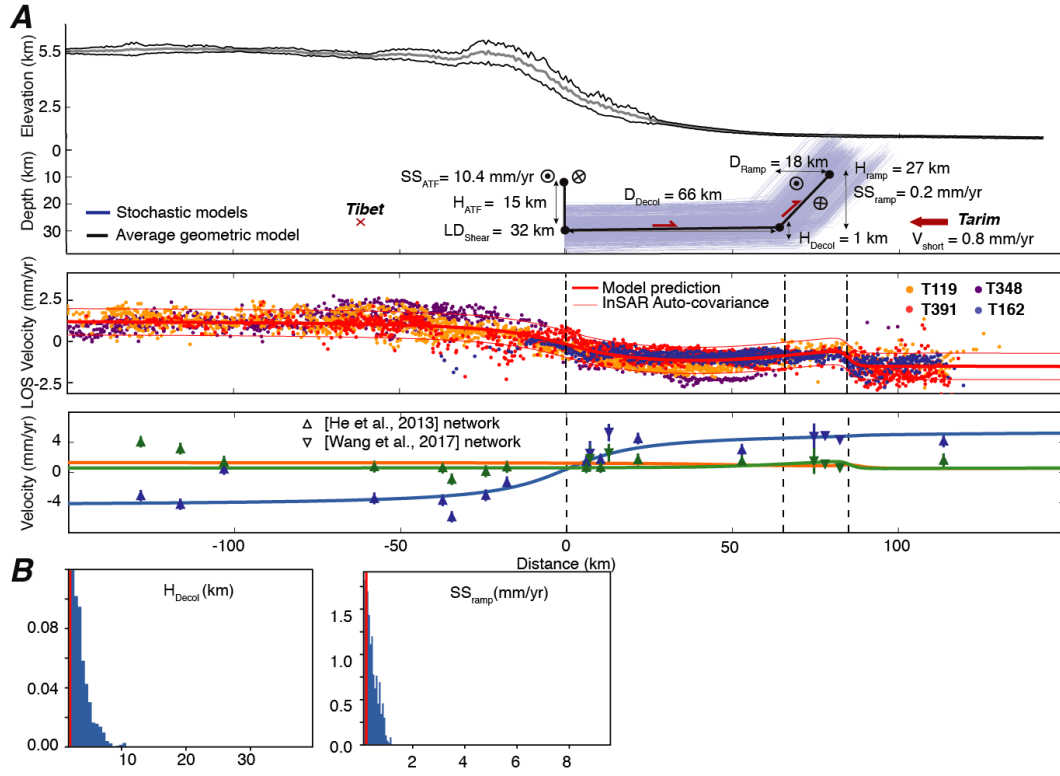


Figure S20. A: As Fig.7A but with a model with more parameters that allows for both strike-slip and dip-slip motion on the ramp-décollement system and for a free décollement dip angle. B: Posterior marginal PDF (blue histograms) for the amount of décollement shallowing, H_{Decol} , and for the strike-slip rate of the ramp, SS_{Ramp} , with plot boundaries corresponding to the uniform prior distributions. Both PDFs indicate an average posterior model close to zero (vertical red lines).

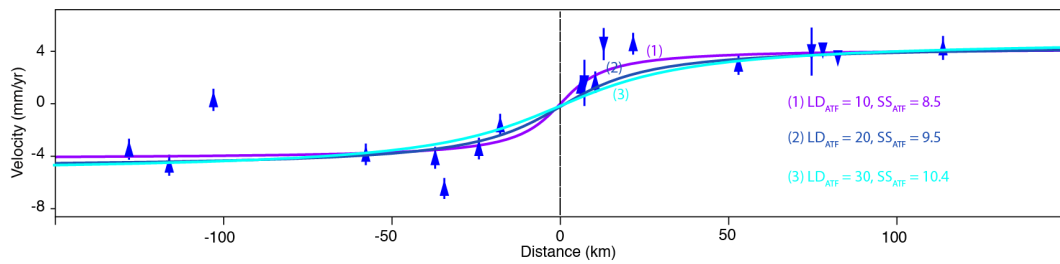


Figure S21. Simple models made of one single strike-slip half-infinite dislocation centered on the ATF with locking depths fixed at 10 (1), 20 (2) and 30 km-depth (3), with fit to GPS fault-parallel velocities (blue triangles). All these models lie within the spread of GPS data, which uncertainties are likely underestimated.

References

- Bekaert, D., A. Hooper, and T. Wright (2015), A spatially-variable power-law tropospheric correction technique for InSAR data, *J. Geophys. Res.: Solid Earth*.
- Daout, S., R. Jolivet, C. Lasserre, M.-P. Doin, S. Barbot, P. Tapponnier, G. Peltzer, A. Socquet, and J. Sun (2016), Along-strike variations of the partitioning of convergence across the Haiyuan fault system detected by InSAR, *GJI*, 205(1), 536–547.
- Daout, S., M.-P. Doin, G. Peltzer, A. Socquet, and C. Lasserre (2017), Large scale InSAR monitoring of permafrost freeze-thaw cycles on the Tibetan Plateau, *Geophys. Res. Lett.*
- Doin, M.-P., C. Lasserre, G. Peltzer, O. Cavalié, and C. Doubre (2009), Corrections of stratified tropospheric delays in SAR interferometry: Validation with global atmospheric models, *J. Applied Geophysics*, 69, 35–50.
- Doin, M.-P., F. Lodge, S. Guillaso, R. Jolivet, C. Lasserre, G. Ducret, R. Grandin, E. Pathier, and V. Pinel (2011), Presentation of the small baseline NSBAS processing chain on a case example : The Etna deformation monitoring from 2003 to 2010 using envisat data., *Proc. ESA Fringe*.
- Doin, M.-P., C. Twardzik, G. Ducret, C. Lasserre, S. Guillaso, and S. Jianbao (2015), InSAR measurement of the deformation around Siling Co Lake: Inferences on the lower crust viscosity in central Tibet, *J. Geophys. Res.: Solid Earth*, 120(7), 5290–5310.
- Ducret, G., M.-P. Doin, R. Grandin, C. Lasserre, and S. Guillaso (2014), DEM corrections before Unwrapping in a Small Baseline Strategy for InSAR Time Series Analysis, *Geoscience and Remote Sensing Letters, IEEE*, 11, 696–700.
- Grandin, R., M.-P. Doin, L. Bollinger, B. Pinel-Puysségur, G. Ducret, R. Jolivet, and S. N. Sapkota (2012), Long-term growth of the Himalaya inferred from interseismic InSAR measurement, *Geology*, 40(12), 1059–1062.
- Hanssen, R. F. (2001), *Radar interferometry: data interpretation and error analysis*, vol. 2, Springer Science & Business Media.
- He, J., P. Vernant, J. Chéry, W. Wang, S. Lu, W. Ku, W. Xia, and R. Bilham (2013), Nail-ing down the slip rate of the Altyn Tagh fault, *Geophys. Res. Lett.*, 40(20), 5382–5386.
- Heimann, S., M. Kriegerowski, M. Isken, S. Cesca, S. Daout, F. Grigoli, C. Juretzek, T. Megies, N. Nooshiri, A. Steinberg, H. Sudhaus, T. Vasyura-Bathke, Hannes; Willey, and T. Dahm (2017), Pyrocko - an open-source seismology toolbox and library., *GFZ Data Services*, doi:http://doi.org/10.5880/GFZ.2.1.2017.001.
- Isken, M., H. Sudhaus, S. Heimann, A. Steinberg, S. Daout, and H. Vasyura-Bathke (2017), Kite - software for rapid earthquake source optimisation from insar surface displacement, *GFZ Data Services*, doi:http://doi.org/10.5880/GFZ.2.1.2017.002.
- Jolivet, R., R. Grandin, C. Lasserre, M.-P. Doin, and G. Peltzer (2011), Systematic InSAR tropospheric phase delay corrections from global meteorological reanalysis data, *Geophys. Res. Lett.*, 38(17).
- Jolivet, R., P. S. Agram, N. Y. Lin, M. Simons, M.-P. Doin, G. Peltzer, and Z. Li (2014), Improving InSAR geodesy using global atmospheric models, *J. of Geophys. Res.: Solid Earth*, 119(3), 2324–2341.
- Lin, Y.-n. N., M. Simons, E. A. Hetland, P. Muse, and C. DiCaprio (2010), A multiscale approach to estimating topographically correlated propagation delays in radar interferograms, *Geochemistry, Geophysics, Geosystems*, 11(9).
- López-Quiroz, P., M.-P. Doin, F. Tupin, P. Briole, and J.-M. Nicolas (2009), Time series analysis of Mexico City subsidence constrained by radar interferometry, *J. Applied Geophysics*, 69(1), 1–15.
- Pinel-Puysségur, B., R. Michel, and J.-P. Avouac (2012), Multi-Link InSAR Time Series: Enhancement of a Wrapped Interferometric Database, *IEEE J. Selected Topics in Applied Earth Observations and Remote Sensing*, 5(3), 784–794.
- Shirzaei, M., and R. Bürgmann (2012), Topography correlated atmospheric delay correction in radar interferometry using wavelet transforms, *Geophys. Res. Lett.*, 39(1).

- Wang, W., X. Qiao, S. Yang, and D. Wang (2017), Present-day velocity field and block kinematics of Tibetan Plateau from GPS measurements, *Geophys.J. Int.*, 208(2), 1088–1102.
- Wen, Y., Z. Li, C. Xu, I. Ryder, and R. Bürgmann (2012), Postseismic motion after the 2001 Mw 7.8 Kokoxili earthquake in Tibet observed by InSAR time series, *J. of Geophys. Res.: Solid Earth*, 117(B8).
- Wessel, P., and W. H. Smith (1991), Free software helps map and display data, *Eos, Trans. AGU*, 72(41), 441–446.